



Measurement and simulation of strain fields around crack tips under mixed-mode fatigue loading

Y. Hos, M. Vormwald

*Technische Universität Darmstadt, Materials Mechanics Group, Franziska-Braun-Str. 3, D-64287 Darmstadt, Germany
vormwald@wm.tu-darmstadt.de*

J.L.F. Freire

Pontifícia Universidade Católica do Rio de Janeiro – PUC, Rio Rua Marquês de São Vicente, 225, Gávea - Rio de Janeiro, RJ, Brasil

ABSTRACT. For various configurations examined in a series of fatigue experiments on thin-walled tubes under tension and torsion, the experimental results – crack path, crack growth life, near crack tip deformations, and crack closure – are measured and compared to the results of some numerical simulations. Partially automated optical inspection and the digital image correlation technique were used in the experimental investigation. In the finite element analyses, an actual geometry of a cracked structure has been modeled. The mechanical material behavior has been assumed as linear elastic in a first approach for calculating stress intensity factors. The non-linear nature of the cyclic deformation has been taken into account by applying a cyclic plasticity model, and plasticity-induced crack closure is captured by a contact formulation.

KEYWORDS. Multiaxial fatigue; Mixed mode; Fatigue crack growth; Digital image correlation.

INTRODUCTION

The fatigue crack growth under non-proportional mixed-mode loading at the crack tip depends on many influence factors, mainly on the mode-mixity. Increasing mode-mixity creates a tendency for a shear dominated crack growth instead of a tensile stress dominated one, the latter being the usual case. With increasing cyclic plastic deformation the shear dominated fatigue crack growth becomes more important. The cyclic plastic deformation is also the origin of the plasticity induced crack closure. Especially in non-proportional cases, the roughness and friction induced crack closure occurs and interacts with the plasticity induced crack closure. These influence factors are closely interrelated, therefore a study of individual factors is hard to achieve.

Originating from information gathered from a literature overview [1], a research project was launched, seeking further knowledge on the mechanisms. Results achieved so far are the subject of this paper. In order to connect the results to the state of the art, the experimental methods are first applied to cases with proportional and mode I dominated fatigue crack growth. Based on these results, ideas are presented which are intended to describe the fatigue crack growth behavior observed in the experiments.

EXPERIMENTAL CAMPAIGN

Constant amplitude fatigue tests have been performed using thin-walled tubes under tension-compression (force F) and torsion (moment M). The specimen geometry is shown in Fig. 1. The specimens were machined from longitudinally welded tubes. The individual specimens were saw-cut and the notches were milled. Two holes, diameter 4 mm, were drilled with the distance of 10 mm of the centers of the holes (length of an arc measured at the outer surface). The notch was positioned opposite to the longitudinal weld. The material was constructional steel S235 with mechanical properties as given in Table 1.

Besides Young's modulus, E , plastic offset stress $R_{p0.2}$, ultimate tensile strength R_m , the parameters of the cyclic stress-strain curve,

$$\epsilon_a = \frac{\sigma_a}{E} + \left(\frac{\sigma_a}{K'} \right)^{\frac{1}{n'}} \quad (1)$$

are given. For use in finite element calculations the cyclic stress-strain curve is reformulated in terms of Chaboche's model [2],

$$\sigma = \sigma_y + \sum_1^5 \left[\frac{C_i}{\gamma_i} (1 - \exp(-\gamma_i \epsilon_{pl})) \right] \quad (2)$$

with the parameters listed in Tab. 2. The graphs of the stress strain relationships are shown in Fig. 2.

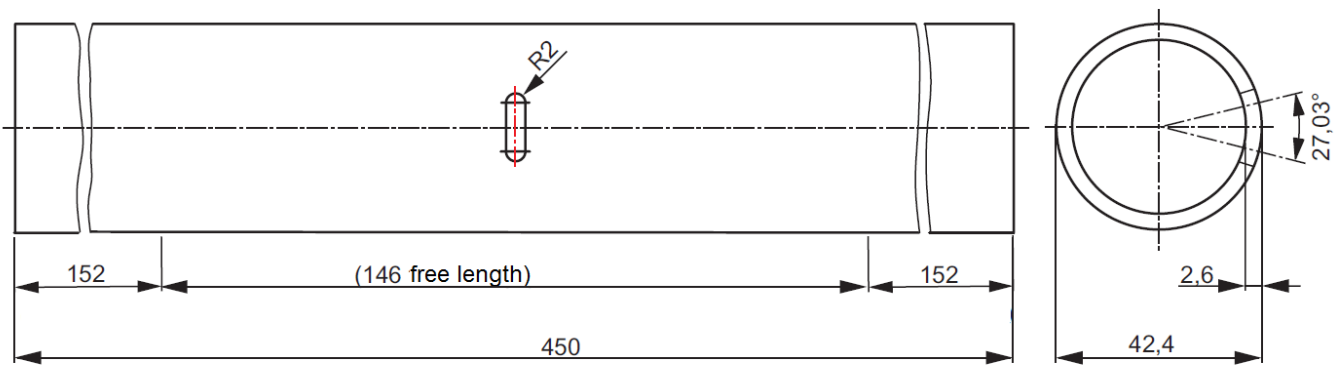


Figure 1: Specimen geometry.

| E [MPa] | $R_{p0.2}$ [MPa] | R_m [MPa] | K' [MPa] | n' |
|-----------|------------------|-------------|------------|-------|
| 214000 | 310 | 435 | 1170 | 0.239 |

Table 1: Mechanical properties of S235 [3].

| σ_y [MPa] | C_1 [MPa] | γ_1 | C_2 [MPa] | γ_2 | C_3 [MPa] | γ_3 | C_4 [MPa] | γ_4 | C_5 [MPa] | γ_5 |
|------------------|-------------|------------|-------------|------------|-------------|------------|-------------|------------|-------------|------------|
| 58.2 | 13442 | 46 | 39134 | 400 | 72245 | 1904 | 603494 | 7404 | 800707 | 104861 |

Table 2: Chaboche parameters for representing the cyclic stress strain curve of S235.

Two series of experiments have been performed. In the first series of experiments the fatigue crack lengths were monitored automatically by taking photographs of the specimen at predefined numbers of applied cycles. Three cameras were installed, one directly facing the slit of width 14 mm from front, one with 45° angle on one side and one with 45° angle on the other side. At regular, pre-defined intervals the test was interrupted automatically. The specimen was unloaded completely. Then, a static load between 60% and 100% of the maximum fatigue load was applied depending on

the non-proportionality of the loading. During the short hold time the cameras took pictures of the specimen's surface. The specimen was unloaded again and the cyclic loading continued. The pictures were inspected after the test. In order to ease the optical evaluation of the crack tip coordinates the specimens were branded with a 1 mm Laser-dot pattern prior to testing.

The five different loading sequences are shown in Fig. 3: pure tension-compression loading, pure torsion loading, proportional loading resulting from the superposition of these two and out-of-phase loading with phase angles of 45° and 90°. The load ratio was $R_F = R_M = -1$. The experiments have been conducted under load control and moment control, respectively, using a servo-hydraulic, four-pillar tension-torsion testing machine with frequencies between 0.1 Hz and 2 Hz. In the air conditioned laboratory a temperature of 21°C and a relative air humidity of 50% were kept constant.

The cracks were assumed to be through-wall cracks with a straight crack front. The crack length is defined as the arc length with the arc starting at the crack initiation location, see Fig. 4. Depending on the loading type, two, three or four cracks were observed. The convention for the naming of the cracks is depicted in Fig. 5. Here, the scheme of presenting the results was adopted from references [4] and [5].

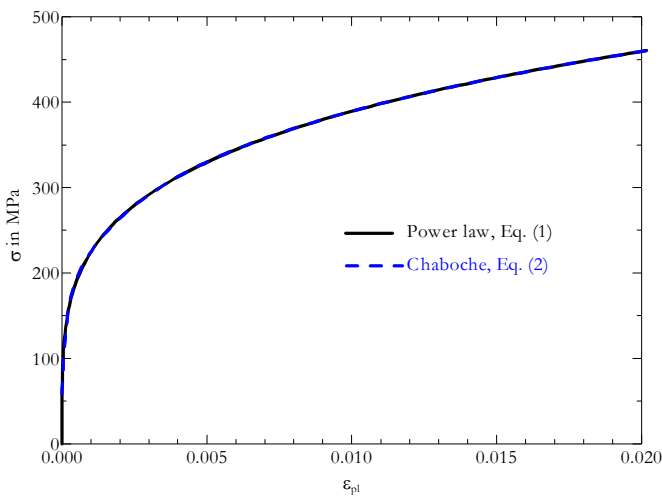


Figure 2: Plastic portion of the cyclic stress-strain curve of S235 [3].

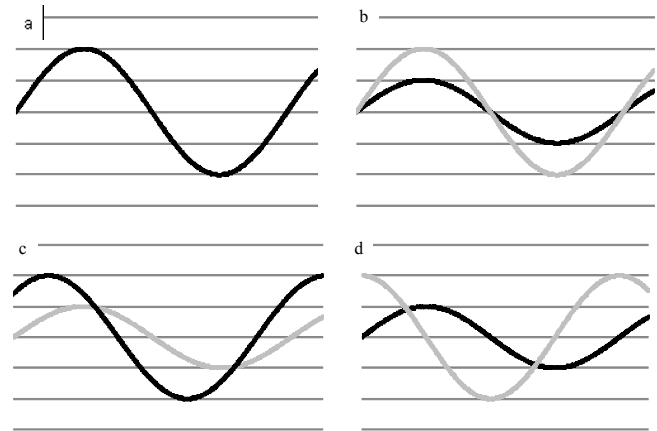


Figure 3: Loading types: (a) pure tension-compression or pure torsional loading, (b) proportional loading, (c) out-of-phase loading with a phase angle of 45°, and (d) out-of-phase loading with a phase angle of 90°.

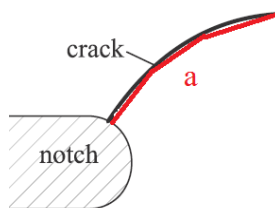


Figure 4: Crack length definition for long cracks.

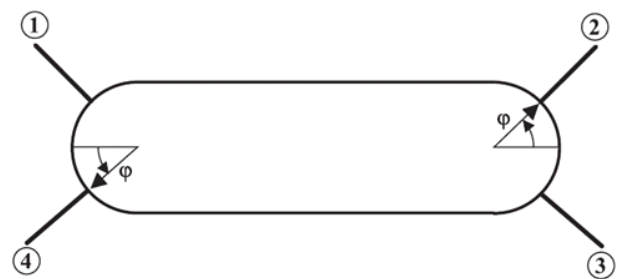


Figure 5: Crack initiation sites, and the naming convention.

In the second series of experiments the tests were occasionally interrupted and the deformation field was measured applying the 3D-digital image correlation (3D-DIC) technique. This technique gains growing interest in measuring materials' mechanical deformation. It allows for measurements of the strain fields also in the vicinity of crack tips [6]. The procedure requires a random grey-scale pattern on the surface of the specimen. Pictures are taken from the surface at various crack lengths. During a small number of cycles (usually three) at a certain crack length the actual loads, F and M , at the instant of the snapshot were recorded and stored together with the corresponding pictures. The evaluation software, see [7], defines small subsets (in the present case they were sized approximately 0.6 mm x 0.6 mm) for which the displacement vector can be identified by comparison of two pictures. The strain field follows from calculating numerically



the derivatives of the displacement field with respect to the coordinates. The near crack tip strain fields were analyzed in order to determine stress intensity factors and crack opening displacements were investigated for identifying crack opening and closure loading states, respectively. More details on the measurement technique can be found in reference [8].

Tension-compression loading

The specimen R-001 has been tested under pure tension-compression loading with $F_{max} = 45\text{ kN}$ and $R_F = -1$. Two symmetric cracks grew in the centre cross section plane, Fig. 6. The crack growth curve is shown in Fig. 7.

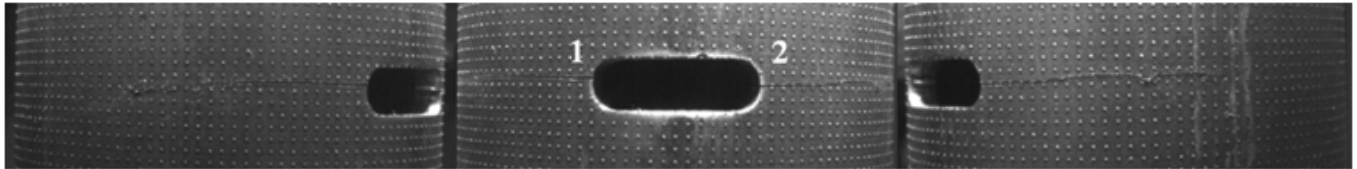


Figure 6: Cracks in the specimen R-001, pure tension-compression with $F_{max} = 45\text{ kN}$ and $R_F = -1$, steel S235.

The test was repeated with specimen R-028. The surface area subject to strain field inspection is highlighted in Fig. 8. Two inspection areas have been defined, one close to the notch and to the initiated crack, and another one in the far field representing a nominal-stressed region. Calculated and measured nominal strains were generally in an extraordinarily good agreement. In the next analysis step the crack tip location has to be identified. This was achieved by observing results provided by the displacement animation tool. Only one snapshot of a movie is presented in Fig. 9 as an example.

The use of digital image correlation (DIC) to determine fracture parameters was earlier proposed by McNeill et al. [9,10] and more recently by Yoneyama and Murasawa [11]. In reference [10] the DIC displacement full-field data was fitted, using the least square technique, to the Westergaard solution [12] for a cracked body problem. In that paper [11] the authors determined not only mode I SIF but also rigid body motion and other far field parameters of the truncated series-type stress function used in the solution. More recently the integral J was evaluated using the DIC technique [13] and the mixed-mode I and II SIFs in an aluminum plate mounted in an Arcan loading fixture were determined using DIC [14].

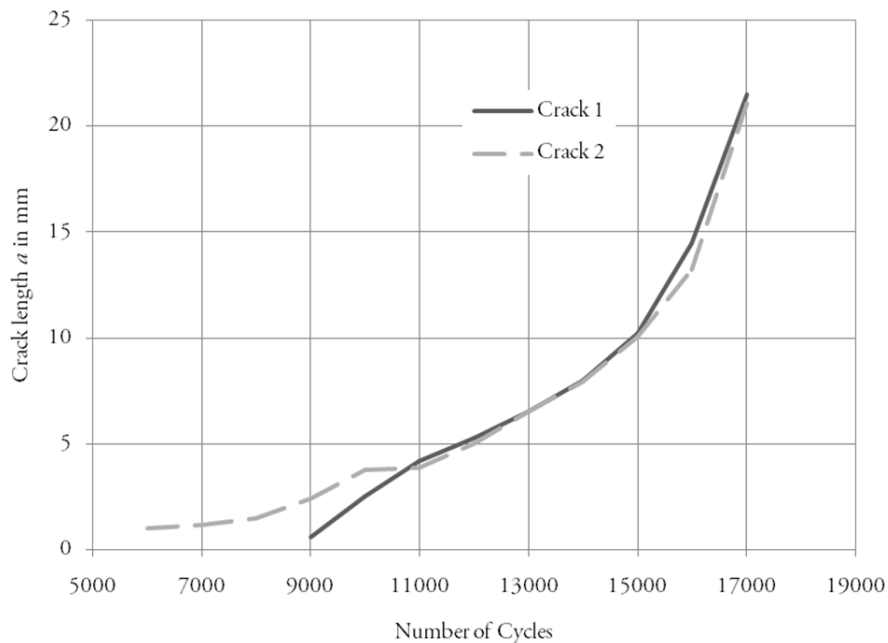


Figure 7: Crack growth curve of specimen R-001, pure tension-compression with $F_{max} = 45\text{ kN}$ and $R_F = -1$, steel S235.

For the calculation of the stress intensity factor, K , at least four data points – C1, C2, B1, B2 – have been defined. Fig. 10 shows best locations. The coordinates of these points have been retrieved in the local coordinate system centered at the crack tip as shown in Fig. 10. The strain values in the local coordinate system, ϵ_{xx} and ϵ_{yy} , have been determined from

each image. The stresses, σ_{xx} and σ_{yy} , were calculated assuming plane stress and Poisson's ratio of $\nu = 0.3$. A least squares fit to Westergaard's equations [12] for mode I cracks,

$$K = \frac{\sigma_{yy} \sqrt{2\pi r}}{\cos \frac{\theta}{2} \left(1 + \sin \frac{\theta}{2} \sin \frac{3\theta}{2} \right)} \quad (3)$$

provided an estimate for the stress intensity factor. The example shown in Fig. 10 resulted in a value of $K = 36.5 \text{ MPa}\sqrt{\text{m}}$ at the applied load of 45 kN (nominal stress $\sigma_n = 138.4 \text{ MPa}$) and the crack tip located 6 mm from the notch root.

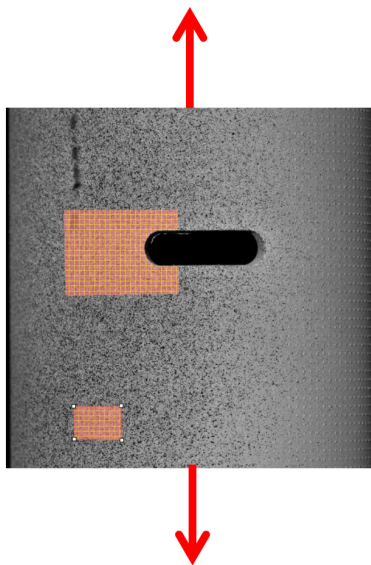


Figure 8: Digital image correlation area of specimen R-028 shown as high-lighted grid.

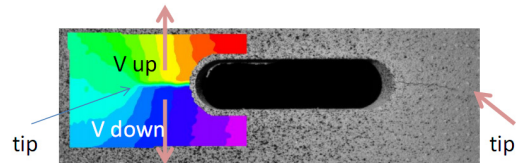


Figure 9: Example of the identification of the crack tip location. Rigid body motion is eliminated from the displacement field.

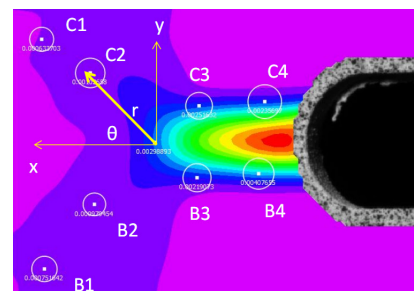


Figure 10: Explanation of the experimental determination of stress intensity factors.

The differences of the displacements between two points, $\delta_i = v(C_i) - v(B_i)$, have been investigated to identify crack closure. The curves for all points i are similar and yield the same information. An example is shown in Fig. 11 for points C4 and B4. Their distance to the crack tip is the largest and therefore the measured displacements are the most pronounced ones. The occurrence of negative crack opening displacements is only an evaluation artifact and results from choosing a reference frame with an already open crack. The regions of the curve showing large curvature or even kinks have their origin in the crack opening and closure behavior. The crack opens at approximately -7 kN and it does not close on the descending hysteresis loop branch before approximately -12 kN. Negative crack opening and closure loads are expected for cases with large cyclic plastic deformation, the focus of the study.

The crack opening profile was studied by letting the evaluation software calculate fictitious strains, ϵ_{yy} , when measuring across the crack flanks. Before plotting any results, the fictitious strains obtained at the minimum loads are subtracted from the strains at all other loads. Results are shown in Fig. 12. The loads for which the profiles are presented are indicated by arrows in Fig. 11. Similar strains are found for +3 kN on the ascending and -1.1 kN on the descending branch as well as for +1.2 kN (ascending) and -6.3 kN (descending). There is a 4 kN difference between opening and closure. Next to the crack tip the crack flanks lose contact latest and reestablish it first. However, not much difference can be found for the time of contact loss and reestablishment for flank points farther away from the tip. The efficiency factor becomes $U = \Delta F_{\text{eff}} / \Delta F \approx 55 \text{ kN} / 90 \text{ kN} \approx 0.6$.

The most important résumé at this point is that digital image correlation is a very well suited tool for crack closure measurement. It provides results which are identical to results obtained with conventional techniques in an application field where both, conventional and DIC-technique are applicable. DIC opens the opportunity to obtain results in applications where other, e.g. strain gage based techniques, fail to provide results.

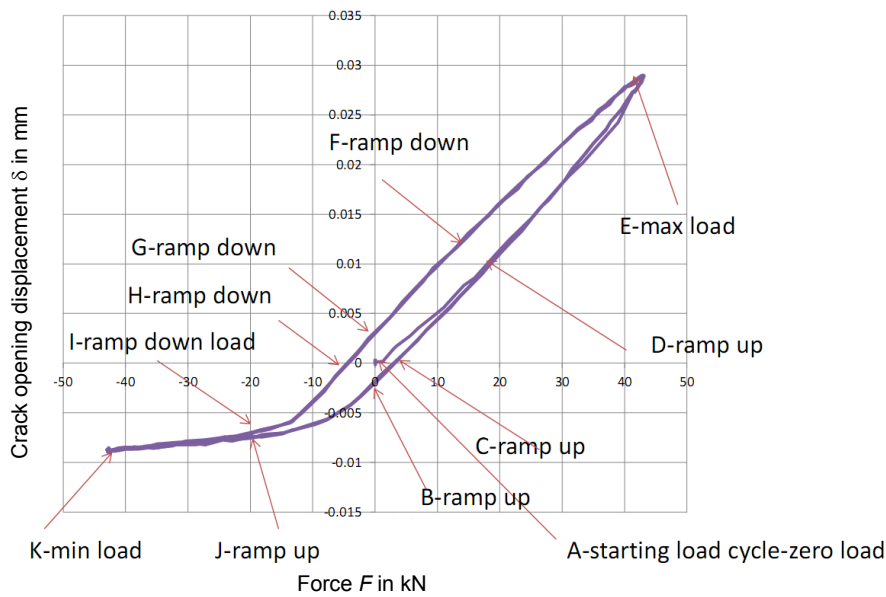


Figure 11: Crack opening displacement as function of the applied load, specimen R-028, pure tension-compression with $F_{max}=45$ kN and $R_F = -1$, steel S235.

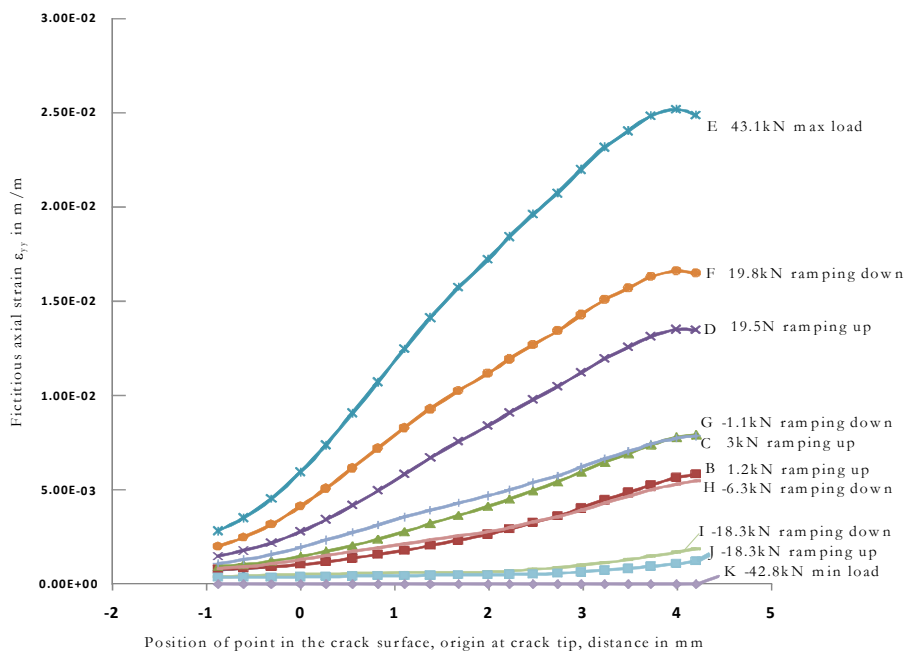


Figure 12: specimen R-028, pure tension-compression with $F_{max}=45$ kN and $R_F = -1$, steel S235.

Torsion loading

The specimen R-003 has been tested under pure torsion loading with $M_{max} = 530$ Nm and $R_M = -1$. Four cracks grew as shown in Fig. 13. The crack growth curve is shown in Fig. 14. The cracks initiate at the locations with the highest stresses. Starting at the initiation site the short cracks grow into a field of uniaxial stresses and their crack fronts are loaded under mode I. The longer ones of the cracks keep growing under 45° to the specimen axis until finally the crack path turns to a direction perpendicular to the specimen axis. The shorter two cracks immediately bend towards a direction perpendicular to the specimen axis.

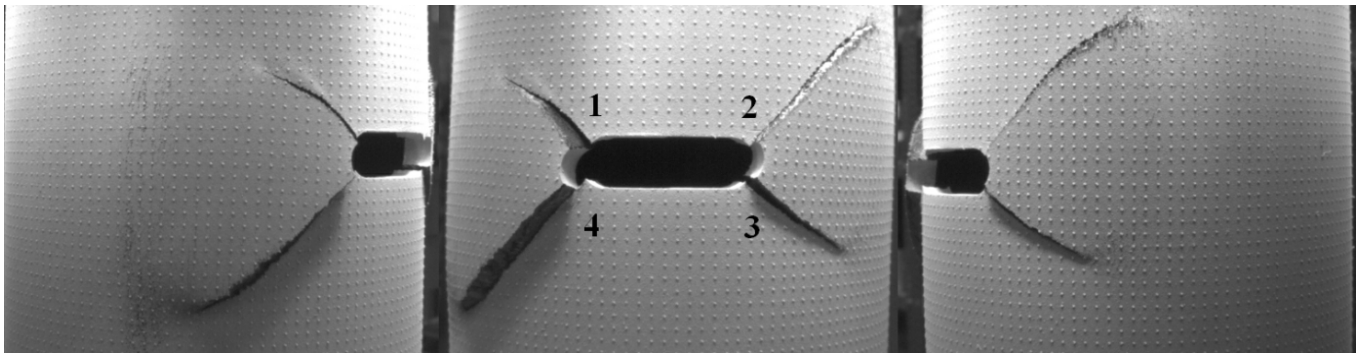


Figure 13: Cracks in the specimen R-003, pure torsion with $M_{\max} = 530 \text{ Nm}$ and $R_M = -1$, steel S235.

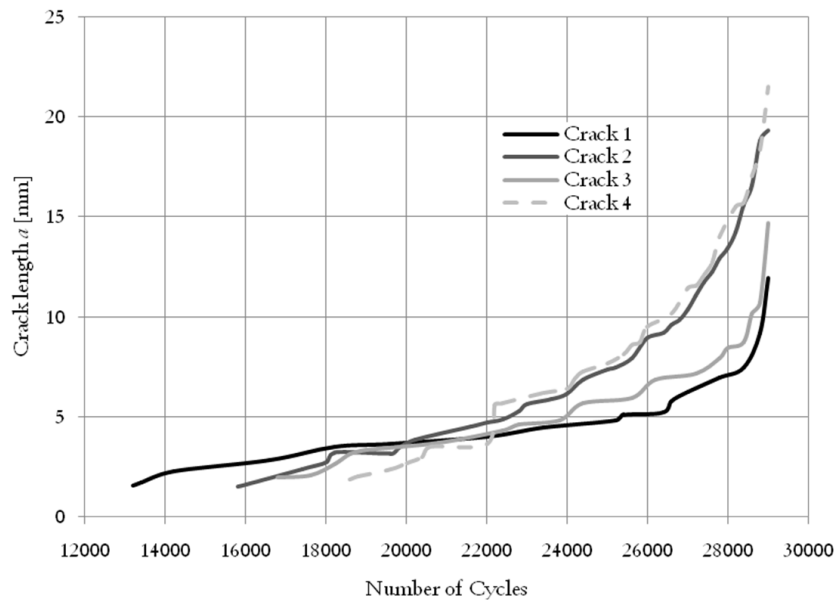


Figure 14: Crack growth curve of specimen R-003, pure torsion with $M_{\max} = 530 \text{ Nm}$ and $R_M = -1$, steel S235.

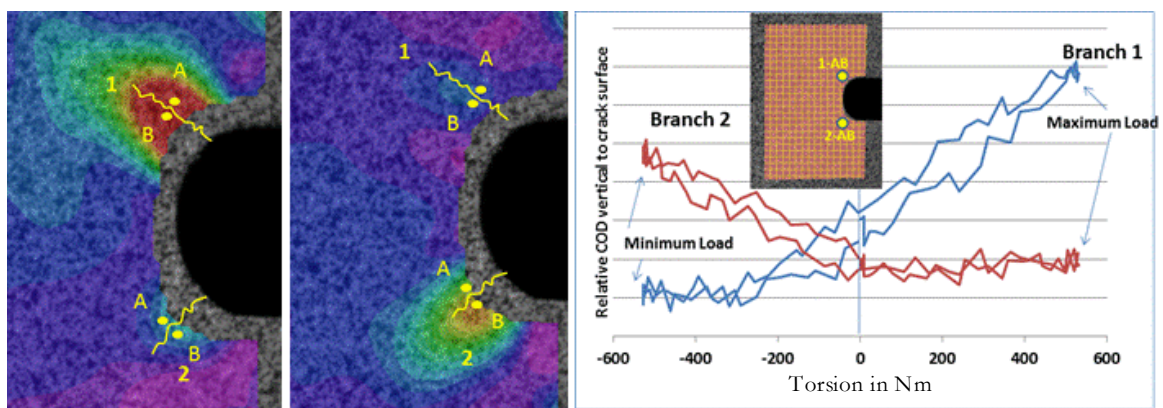


Figure 15: Crack closure of specimen R-029, pure torsion with $M_{\max} = 530 \text{ Nm}$ and $R_M = -1$, steel S235.

For the inspection of crack closure (specimen R-029, $M_{\max} = 530 \text{ Nm}$ and $R_M = -1$) the one pair of data points A and B for each crack branch were taken into consideration, Fig. 15. The artificially highlighted crack branches show that the lengths of the cracks are different, with direct consequence on their displacements and individual stress intensity factors



(SIF). Two pairs of data points (A and B, A' and B') for each crack branch were taken into consideration in the calculations of fracture parameters, as for example stress intensity factors. A larger number of data points along the surface of each crack branch would generate more results on the occurrence of crack closure at various positions along the crack flanks. It can be concluded that under positive moments the crack 1 opens and crack 2 closes and vice versa. Please note that crack 1 is the longer one in specimen R-029. In the test under identical conditions the crack 1 was shorter than crack 4, Fig. 13. In the unloaded state both cracks are open. The closure-free effective range is about $\Delta M_{\text{eff}} \approx 530 \text{ Nm} + 200 \text{ Nm} = 730 \text{ Nm}$. The efficiency factor becomes $U = \Delta M_{\text{eff}} / \Delta M \approx 0.7$.

Proportional loading

The specimen R-004 has been tested under proportional loading with $F_{\text{max}} = 33 \text{ kN}$, $M_{\text{max}} = 382 \text{ Nm}$ and $R_F = R_M = -1$. Two cracks initiated at the location of highest notch stresses, Figs. 16 and 17. The nominal stresses in the gross section are $\sigma_{n,\text{max}} = 101.5 \text{ MPa}$ and $\tau_{n,\text{max}} = 62.6 \text{ MPa}$. The principal axis is 25.5° inclined against the specimen axis. The crack growth direction, however, is only inclined approximately 14° against the cross section plane. Some cyclic mode II loading could have contributed to the fatigue crack growth.

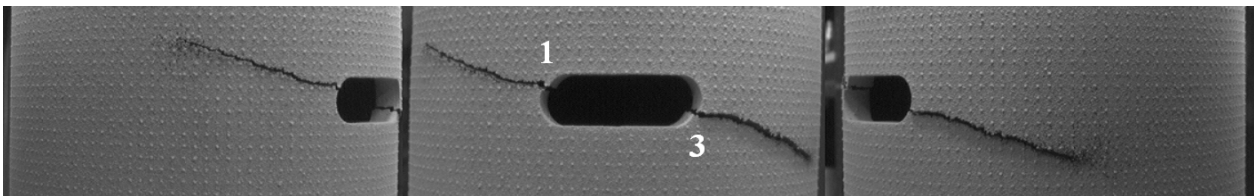


Figure 16: Cracks in specimen R-004, proportional loading with $F_{\text{max}} = 33 \text{ kN}$, $M_{\text{max}} = 382 \text{ Nm}$ and $R_F = R_M = -1$, steel S235.

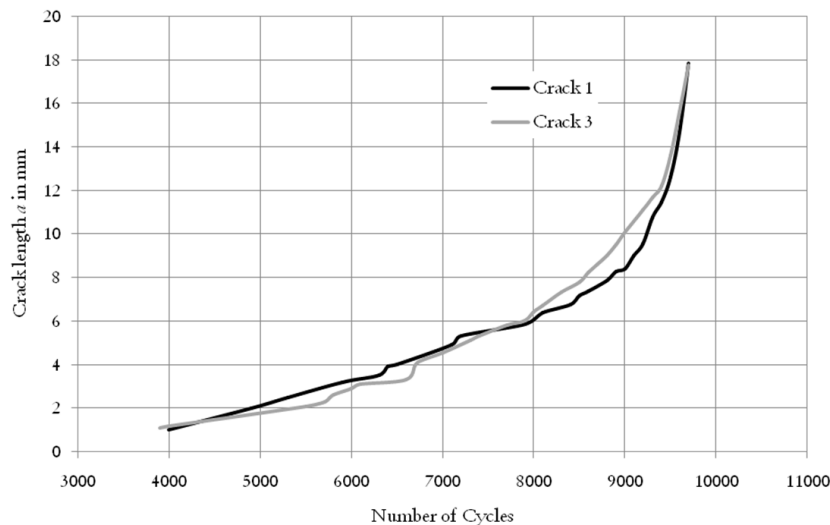


Figure 17: Crack growth curve of specimen R-004, proportional loading with $F_{\text{max}} = 33 \text{ kN}$, $M_{\text{max}} = 382 \text{ Nm}$ and $R_F = R_M = -1$, steel S235.

The specimen R-030 was loaded under identical conditions as specimen R-004. Fig. 18 illustrates the analysis where two pairs of data points (A and B, A' and B') for each crack branch were taken into consideration. SIF results of $K_I = 40 \text{ MPa}\sqrt{\text{m}}$ and $K_{II} = 31 \text{ MPa}\sqrt{\text{m}}$ for $a_1 = 3.8 \text{ mm}$ and $K_I = 46 \text{ MPa}\sqrt{\text{m}}$ and $K_{II} = 26 \text{ MPa}\sqrt{\text{m}}$ for $a_2 = 4.4 \text{ mm}$ are the average results determined for these A-B and A'-B' pairs. A larger number of data points along the surface of each crack branch would again generate a more proper average result. As a conclusion drawn here from displacement measurements, the cracks grow under a mode mixity of $0.57 < K_{II}/K_I < 0.78$. The inspection of the strains orthogonal to the crack flank led to the conclusion that the efficiency factor is approximately $U = 0.55$, see Fig 19.

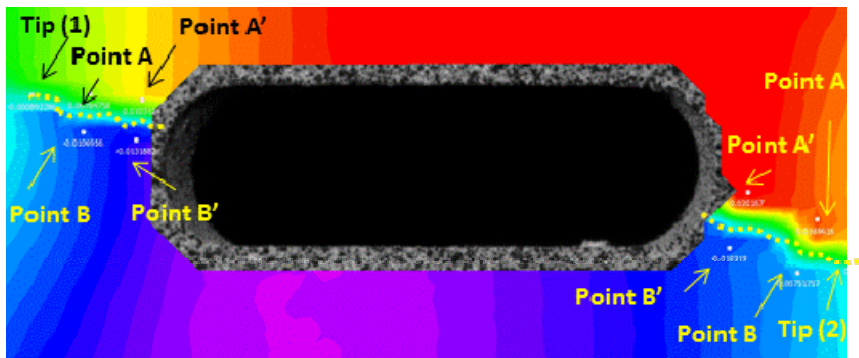


Figure 18: Displacement field of specimen R-030 at maximum axial and torsion load, proportional loading with $F_{\max} = 33\text{kN}$, $M_{\max} = 382\text{Nm}$ and $R_F = R_M = -1$, steel S235.

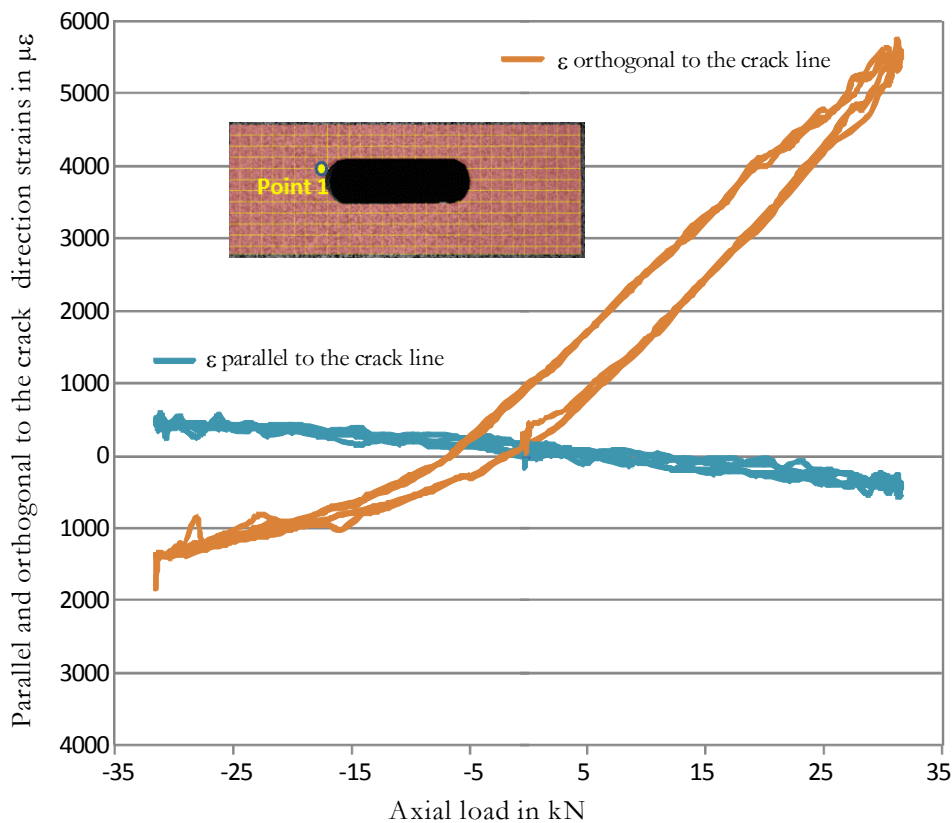


Figure 19: Crack opening strains of specimen R-030 at point 1. Short crack has already initiated. Three cycles history after 11000 cycles of proportional tension-torsion load with $F_{\max} = 33\text{kN}$, $M_{\max} = 382\text{Nm}$ and $R_F = R_M = -1$, steel S235.

Out-of phase loading with a phase angle 45°

The specimen R-006 has been tested under out-of-phase loading with phase angle 45° . The same amplitudes have been applied as in the proportional case, $F_{\max} = 33\text{kN}$, $M_{\max} = 382\text{Nm}$ and $R_F = R_M = -1$. Again, two cracks initiated at the notch, Fig. 20. Only for the very early stage of short fatigue crack growth it can be assumed that the crack grows in the uniaxial stress field prevailing at the notch surface. During the cracks' further growth the crack front is subjected to non-proportional mixed mode. The comparison of Figs. 16 and 20 shows the different crack paths. Under out-of-phase loading with phase angle 45° crack 1 is inclined in average 26° during its first 13 mm of growth and afterwards turns to a direction perpendicular to the specimen axis. Contrary to crack 1 the crack 3 shows an initial steep crack path inclined 58° against the cross section plane. After 12 mm of crack growth a sharp kink to the cross section plane growth occurs. The



stepwise crack growth, see Fig. 21, is related to the various kinks in the crack growth direction. After the occurrence of a kink the growth rate is decelerated. As a consequence of the variety of kinks the crack surface becomes very rough. In total, the crack growth is slower than under proportional loading which might be due to increased roughness induced crack closure. The frequency of kinks and the unsymmetrical growth of the two cracks may indicate that the crack path has at least two options for choice which are nearly equilibrated. In its early stage the mode I growth around the notch surface dominates. With increasing crack length a fracture mode II gains priority and is enforced after approximately 13 mm of crack growth. The strain field examinations are pending.

Out-of phase loading with a phase angle 90°

The specimen R-005 has been tested under out-of-phase loading with phase angle 90°. Again, the same amplitudes have been applied as in the proportional and the 45° out-of-phase case, $F_{\max} = 33\text{kN}$, $M_{\max} = 382\text{Nm}$ and $R_F = R_M = -1$. The fatigue crack initiation life is the longest one. This might be due to a decoupling of local stresses in the notch. The two cracks show again an unsymmetrical growth behavior, Fig. 22. While crack 1 grows straightly at nearly 45° inclined to the specimen axis, crack 3 starts curving almost immediately after initiation. The options hypothesis received support. The crack growth life under the 90° out-of-phase loading is also slower than under the 45° out-of-phase loading, Fig. 23. However, there is no longer a decoupling as soon as the crack tip has grown out of the notch area.

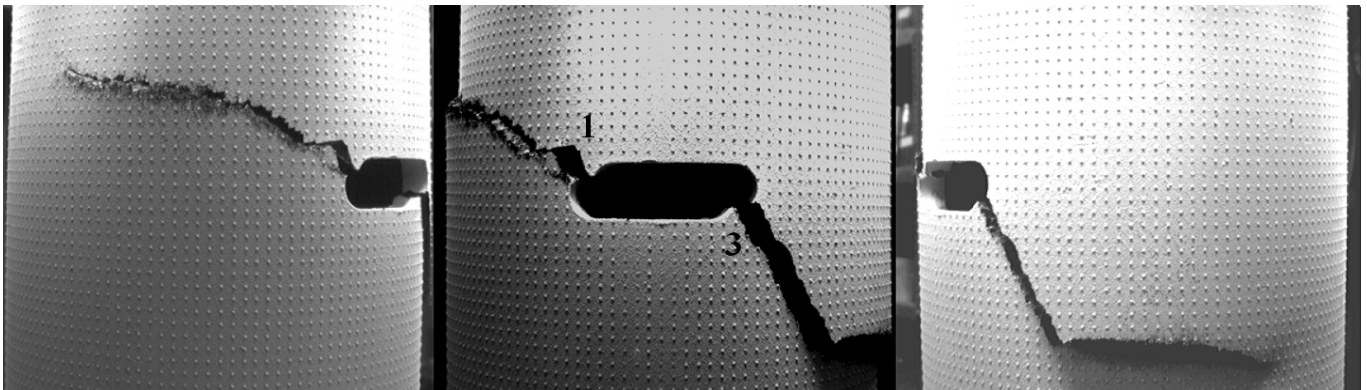


Figure 20: Cracks in specimen R-006, out-of-phase loading with $F_{\max} = 33\text{kN}$, $M_{\max} = 382\text{Nm}$ and $R_F = R_M = -1$, phase angle 45°, steel S235.

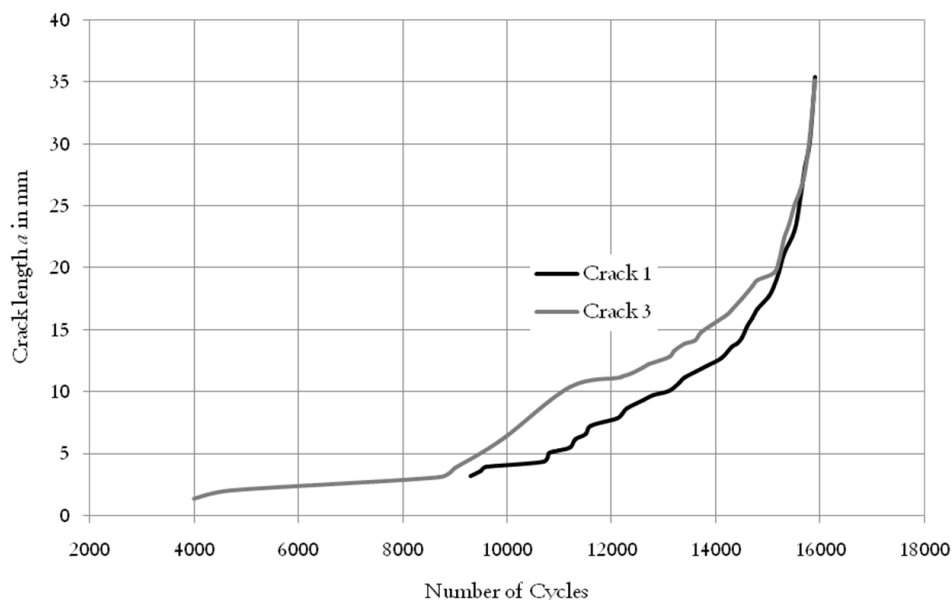


Figure 21: Crack growth curve of specimen R-004, out-of-phase loading with $F_{\max} = 33\text{kN}$, $M_{\max} = 382\text{Nm}$ and $R_F = R_M = -1$, phase angle 45°, steel S235.

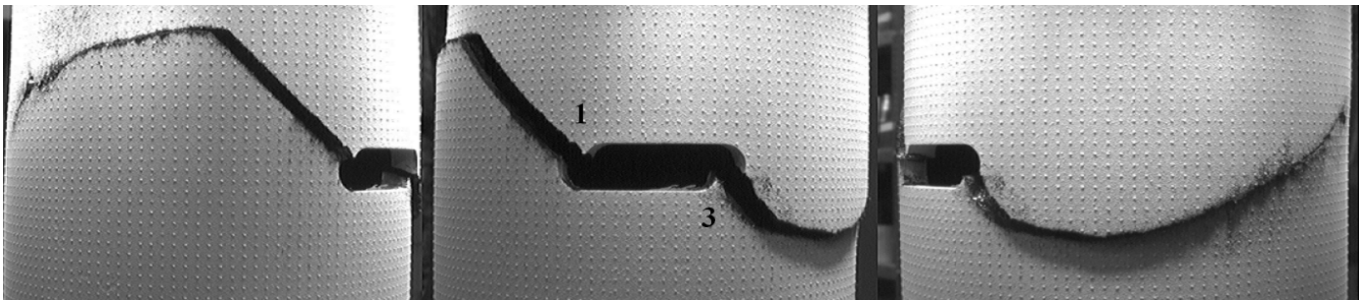


Figure 22: Cracks in specimen R-005, out-of-phase loading with $F_{\max} = 33\text{ kN}$, $M_{\max} = 382\text{ Nm}$ and $R_F = R_M = -1$, phase angle 90° , steel S235.

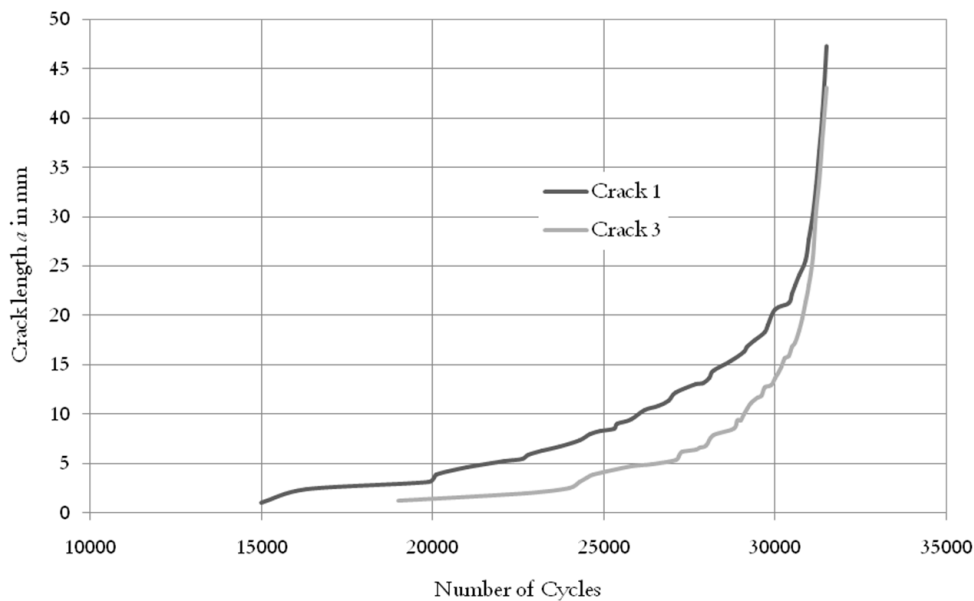


Figure 23: Crack growth curve of specimen R-004, out-of-phase loading with $F_{\max} = 33\text{ kN}$, $M_{\max} = 382\text{ Nm}$ and $R_F = R_M = -1$, phase angle 90° , steel S235.

The test was repeated for crack tip field inspection with specimen R031. The crack at the left side of the notch decided to initiate at the coequal bottom half site. Crack growth was straight for the first 30500 cycles. Crack kinking occurred between the load cycle numbers 30500 and 32000. At these cycle numbers (amongst others) the test was interrupted. For the next three cycles after the interruption the displacement fields were measured and analyzed with the DIC technique. The test was continued without applying DIC until the next interruption. Figure 24 shows snapshots of evaluated strains ϵ_{yy} . The x -axis of the evaluation coordinate system is aligned with the crack growth direction. The crack tip is located at point P0. Please note that calculated strains across the crack surface are pseudo strains. They give an indication of crack opening when positive and of crack closure when negative. Their absolute values are meaningless unless the measuring basis is provided.

At the loading combination of $F = 18\text{ kN}$ and $M = -319\text{ Nm}$ the crack is found to open widest. At the loading combination of $F = 20\text{ kN}$ and $M = 304\text{ Nm}$ first contact at the notch root becomes visible. Not before the loading combination of $F = -10\text{ kN}$ and $M = 364\text{ Nm}$ is reached, the crack is only partly closed. Opening starts at the notch root under a loading combination of $F = -20\text{ kN}$ and $M = -304\text{ Nm}$. For all prior cycles the situation concerning the crack opening and closure behavior is similar. Figure 24 shows only the mode I related crack opening strains ϵ_{yy} . Besides, during the complete cycle, mode II related deformations are observed even when the crack surfaces are in contact. Under the situation shown in Fig. 24 the crack decides to kink. Effective ranges of the crack driving forces – opening mode related and combined – are of next interest in near future research.

Figure 25 shows the situation after kinking has occurred and the crack has grown in its new direction for some millimeters. The inclination of the crack growth direction with the cross section plane is now only 13° where it has been

45° before kinking. Now the maximum mode I opening occurs under the maximum axial force. First and last contact at the notch root still belongs to similar loading combinations as those before kinking. The complete contact at the crack tip, however, is reached later during a cycle at a loading combination of $F = -20\text{kN}$ and $M = 304\text{Nm}$. More compressive loads are required to close the crack in the region between the kink and the tip. Animations showing the results discussed in Figure 24 and 25 for the complete cycles are provided by two links.

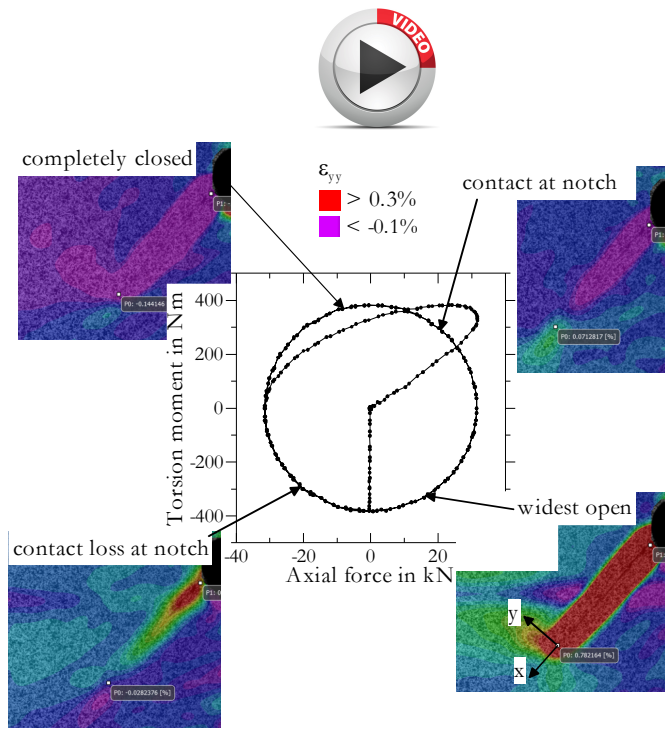


Figure 24: Strain fields of specimen R-031, out-of-phase loading with $F_{\max} = 33\text{kN}$, $M_{\max} = 382\text{Nm}$ and $R_F = R_M = -1$, phase angle 90° , steel S235, after 30500 cycles.

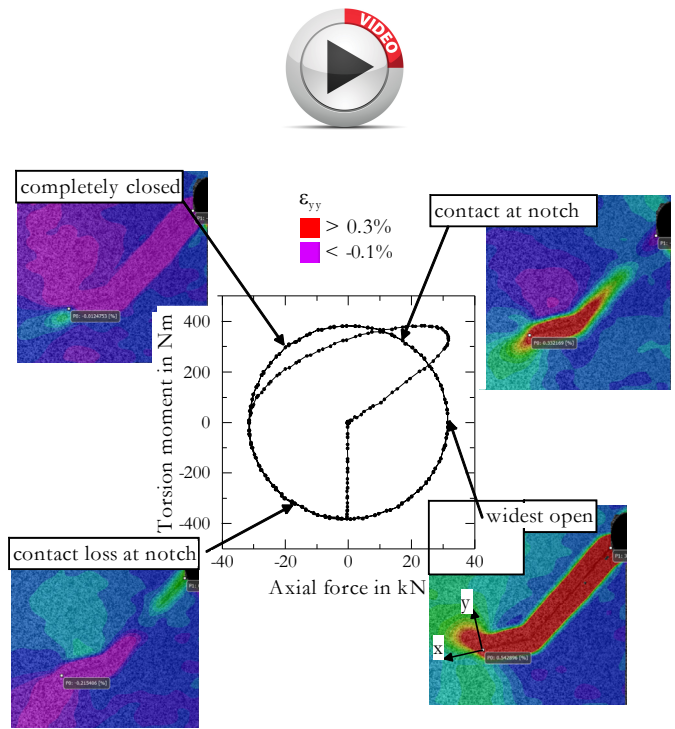


Figure 25: Strain fields of specimen R-031, out-of-phase loading with $F_{\max} = 33\text{kN}$, $M_{\max} = 382\text{Nm}$ and $R_F = R_M = -1$, phase angle 90° , steel S235, after 32000 cycles.

NUMERICAL INVESTIGATION

The finite element code Abaqus was used in the numerical study. Linear elastic deformation behavior was selected for calculating stress intensity factors. The Chaboche kinematic hardening model as implemented in Abaqus was used for elastic-plastic analyses, Eq. (2).



Figure 26: Example for the calculation of stress intensity factors, here vertical displacements of a 6mm crack, compare with Fig. 8, red color means displacements larger than $29\mu\text{m}$.

Stress intensity factor

Fig. 26 show a finite element mesh (as an example) which was used for calculating the stress intensity factor for the crack of length 6 mm from the notch root under tension. The software's post-processing via the J-integral was used. For the example discussed above, applied load of 45 kN (nominal stress $\sigma_n = 138.4\text{MPa}$), the calculated stress intensity factor

ended up in a value of $K = 39.5 \text{ MPa}\sqrt{\text{m}}$. This is very close to the measured value. It was expected that the measured values would be larger than the ones determined by assuming linear elastic material behavior. In the notch and crack region of the real specimen considerably large cyclic plastic deformations occur which provide larger crack opening displacements than in a purely linear elastic case.

Crack closure

A nodal release scheme has been set up for calculating plasticity induced crack closure for a crack of length 6 mm grown under tension/compression with $F_{\max} = 45 \text{ kN}$ and $R_F = -1$. The simulation started with three cycles applied to the uncracked structure. At maximum load of the next cycle, a crack growth step for 1 mm crack advance was executed. For this purpose the boundary condition of the relevant nodes on the crack growth plane was changed from fixed to unrestrained. Additionally, a contact plane was inserted at the new crack surface to prevent negative displacements of the crack surface nodes during subsequent cyclic loading. After the new equilibrium was found three cycles without crack growth were calculated. The node release procedure – 1 mm crack growth followed by three cycles – was repeated until reaching 5 mm crack length. Further repetitions of this scheme followed until reaching a crack length of 6 mm. However, the crack growth per repetition was continuously reduced. Growth steps of 0.5 mm, 0.25 mm and two times 0.125 mm were used.

In Fig. 27 the displacement of the first node on the crack flank is plotted over the applied force for the three cycles following the node release to the crack length of 6 mm. Additionally, the results of crack opening displacements measured by digital image correlation are included.

Severe cyclic plastic deformation is observed in the numerical results. The severe cyclic plastic deformation is accompanied by a severe ratcheting. The crack opening displacements increase from cycle to cycle without any trend of stabilization. This behavior is typical for the Chaboche model. As a consequence of the large ratcheting the crack opening and closure loads are too low. The crack opens at less than -20 kN and closed at about -35 kN. This is in bad accordance with the experimental finding. Before dealing with the more complicated combined loading cases a realistic cyclic plasticity model has to be implemented. Such models are available [15-17]; however, their application requires determination of material's ratcheting behavior first and identification of the corresponding material parameters second. Such work is ongoing.

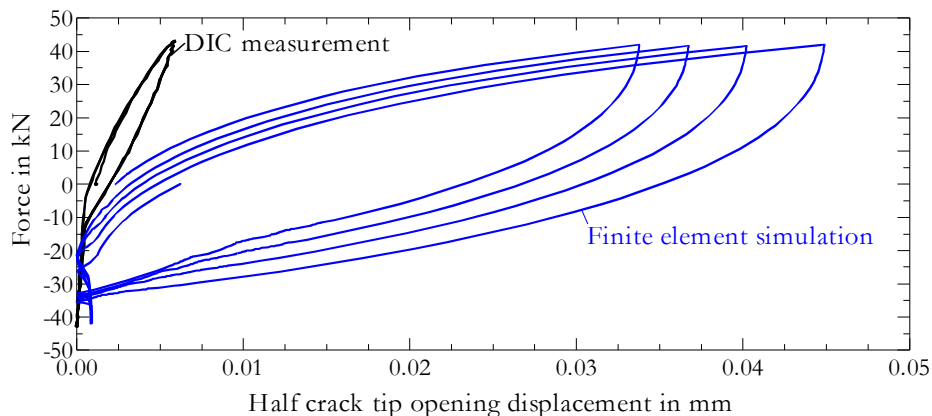


Figure 27: Crack tip opening displacement as function of the applied load, specimen R-028, pure tension-compression with $F_{\max} = 45 \text{ kN}$ and $R_F = -1$, steel S235, crack length 6 mm. Measured by digital image correlation (black) and calculated by a finite element based node release scheme applying Chaboche's plasticity model [2] and parameters according to Tab. 2.

CONCLUSIONS

Fatigue crack growth under combined loading cases – especially cases with non-proportional loading – lead to paths and lives which are not fully understood. A closer look to the deformation fields in the neighborhood of the crack tip is intended to provide more insight into the ongoing mechanisms. For this purpose the feasibilities of digital image correlation were checked. The method provides an excellent opportunity for gaining a relatively high resolution access to the deformations. The focus was laid here on checking whether crack driving force information can be obtained



for cases which are relatively well known. The check results are very positive. Not only reasonable estimates of the crack driving force were obtained but also it could be confirmed that some numerical simulation procedures are unreliable. In the ongoing work, the huge bulk of information coming from both measurements and simulations will be analyzed intending to improve the understanding of non-proportional mixed mode fatigue crack growth.

ACKNOWLEDGEMENT

The German Research Foundation (Deutsche Forschungsgemeinschaft) is greatly acknowledged by the authors for financial support under grant Vo729/13-1.

REFERENCES

- [1] Zerres, P., Vormwald, M., Review of fatigue crack growth under non-proportional mixed-mode loading, *International Journal of Fatigue* 58, (2014) 75–83.
- [2] Chaboche, J.L., Dang Van, K., Cordier, G., Modelization of the strain memory effect on the cyclic hardening of 316 stainless steel, In: 5th Int. Conf. Struct. Mech. in Reactor Techn., L (1979) L11/3.
- [3] Boller, Chr., Seeger, T., *Materials data for cyclic loading*, Elsevier, 1 (1987).
- [4] Zerres, P., Brüning, J., Vormwald, M., Risswachstumsverhalten der Aluminiumlegierung AlMg4.5Mn unter proportionaler und nichtproportionaler Schwingbelastung, *Materials Testing*, 53 (2011) 109-117.
- [5] Zerres, P., Brüning, J., Vormwald, M., Fatigue crack growth behavior of fine-grained steel S460N under proportional and non-proportional loading, *Engineering Fracture Mechanics*, 77 (2010) 1822-1834.
- [6] Lorenzino, P., Beretta, G., Navarro, A., Application of Digital Image Correlation (DIC) in resonance machines for measuring fatigue crack growth, *Frattura ed Integrità Strutturale*, 30 (2014) 369-374; DOI: 10.3221/IGF-ESIS.30.44.
- [7] <http://www.correlatedsolutions.com/> accessed on 13th February 2015.
- [8] Hos, Y., Vormwald, M., Freire, J.L.F., Using digital image correlation to determine mixed mode stress intensity factors in fatigue cracks, In: Proceedings of COTEQ 2015, Conference on Technology of Equipment, organized by ABENDI, Brazilian Society for NDT and Inspection, (2015).
- [9] McNeill, S.R., Peters, W.F., Ranson, W.F., Sutton, M.A., A Study of Fracture Parameters by Digital Image Processing, In: Proc. 18th Midwestern Mechanics Conference, (1983) 267-271.
- [10] McNeill, S.R., Peters, W.F., Sutton, M.A., Estimation of stress intensity factor by digital image correlation, *Engineering Fracture Mechanics*, 28(1) (1987) 101-112.
- [11] Yoneyama, S., Murasawa, G., Digital Image Correlation, in *Experimental Mechanics*, [Ed. Jose Luiz de França Freire], in *Encyclopedia of Life Support Systems (EOLSS)* (2009), Developed under the Auspices of the UNESCO, Eolss Publishers, Oxford, UK, [<http://www.eolss.net>].
- [12] Westergaard, H.M., Bearing Pressures and Cracks, *J. Applied Mechanics*, 6 (1939) A49-A53.
- [13] Vavrik, D., Jandjsek, I., Experimental evaluation of contour J-integral and energy dissipated in the fracture process zone, *Engineering Fracture Mechanics*, 129 (2014) 14-25.
- [14] Zhang, R., He, I., Measurements of mixed-mode stress intensity factors using digital image correlation method, *Optics and Lasers in Engineering*, 50 (2012) 1001-1007.
- [15] Herz, E., Hertel, O., Vormwald, M., Numerical simulation of plasticity induced fatigue crack opening and closure for autofrettaged intersecting holes. *Engineering Fracture Mechanics*, 78 (3) (2011) 559-572.
- [16] Herz, E., Thumser, R., Bergmann, J.W., Vormwald, M. Endurance limit of autofrettaged Diesel-engine injection tubes with defects. *Engineering Fracture Mechanics*, 73 (2006) 3-21.
- [17] Döring, R., Hoffmeyer, J., Seeger, T., Vormwald, M., A Plasticity Model for Calculating Stress-Strain Sequences Under Multiaxial Nonproportional Cyclic Loading. *Computational Material Science*, 28 (2003) 587-596.